Chemical Science

RSC Publishing

EDGE ARTICLE

View Article Online
View Journal | View Issue

Cite this: *Chem. Sci.*, 2013, **4**, 3917

A mononuclear nonheme iron(III)–peroxo complex binding redox-inactive metal ions†

Yong-Min Lee,‡[a] Suhee Bang,‡[a] Yun Mi Kim,‡[a] Jaeheung Cho,[ab] Seungwoo Hong,[a] Takashi Nomura,[c] Takashi Ogura,[c] Oliver Troeppner,[d] Ivana Ivanović-Burmazović,[d] Ritimukta Sarangi,*[e] Shunichi Fukuzumi*[af] and Wonwoo Nam*[a]

Redox-inactive metal ions that function as Lewis acids play pivotal roles in modulating reactivities of oxygen-containing metal complexes in a variety of biological and biomimetic reactions, including dioxygen activation/formation and functionalization of organic substrates. Mononuclear nonheme iron(III)–peroxo species are invoked as active oxygen intermediates in the catalytic cycles of dioxygen activation by nonheme iron enzymes and their biomimetic compounds. Here, we report mononuclear nonheme iron(III)–peroxo complexes binding redox-inactive metal ions, $[(TMC)Fe^{III}(O_2)]^+$–M^{3+} ($M^{3+} = Sc^{3+}$ and Y^{3+}; TMC = 1,4,8,11-tetramethyl-1,4,8,11-tetraazacyclotetradecane), which are characterized spectroscopically as a 'side-on' iron(III)–peroxo complex binding a redox-inactive metal ion, $(TMC)Fe^{III}$–$(\mu,\eta^2{:}\eta^2\text{-}O_2)$–$M^{3+}$ (**2**–M). While an iron(III)–peroxo complex, $[(TMC)Fe^{III}(O_2)]^+$, does not react with electron donors (*e.g.*, ferrocene), one-electron reduction of the iron(III)–peroxo complexes binding redox-inactive metal ions occurs readily upon addition of electron donors, resulting in the generation of an iron(IV)–oxo complex, $[(TMC)Fe^{IV}(O)]^{2+}$ (**4**), *via* heterolytic O–O bond cleavage of the peroxide ligand. The rates of the conversion of **2**–M to **4** are found to depend on the Lewis acidity of the redox-inactive metal ions and the oxidation potential of the electron donors. We have also determined the fundamental electron-transfer properties of **2**–M, such as the reduction potential and the reorganization energy in electron-transfer reaction. Based on the results presented herein, we have proposed a mechanism for the reactions of **2**–M and electron donors; the reduction of **2**–M to the reduced species, $(TMC)Fe^{II}$–(O_2)–M^{3+} (**2′**–M), is the rate-determining step, followed by heterolytic O–O bond cleavage of the reduced species to form **4**. The present results provide a biomimetic example demonstrating that redox-inactive metal ions bound to an iron(III)–peroxo intermediate play a significant role in activating the peroxide O–O bond to form a high-valent iron(IV)–oxo species.

Received 3rd July 2013
Accepted 22nd July 2013

DOI: 10.1039/c3sc51864g

www.rsc.org/chemicalscience

Introduction

Metal–dioxygen adducts, such as metal–peroxo ($M–O_2$) species, are invoked as active oxygen intermediates in enzymatic reactions incorporating oxygen atoms into newly biosynthesized molecules as well as in the deleterious reactions of biological oxidative stress and enzymatic detoxification reactions of reactive oxygen species. Mononuclear nonheme iron(III)–peroxo species are often detected in the activation of dioxygen by nonheme iron enzymes,[1–7] and the structural and chemical properties of the intermediates have been intensively investigated in enzymatic and biomimetic reactions.[8] Very recently, a mononuclear nonheme iron(III)–peroxo complex bearing a macrocyclic *N*-tetramethylated cyclam ligand, $[(TMC)Fe^{III}(O_2)]^+$ (TMC = 1,4,8,11-tetramethyl-1,4,8,11-tetraazacyclotetradecane), was synthesized and characterized with various spectroscopic techniques and X-ray crystallography.[9–11] It was also shown that the iron(III)–peroxo complex is converted to an iron(III)–hydroperoxo complex, $[(TMC)Fe^{III}(OOH)]^{2+}$, upon protonation, and then the latter intermediate cleanly converts to an iron(IV)–oxo complex, $[(TMC)Fe^{IV}(O)]^{2+}$, *via* O–O bond cleavage of the hydroperoxo ligand.[10,11] Thus, success of the generation and isolation of the thermally stable [(TMC)

[a]*Department of Bioinspired Science, Department of Chemistry and Nano Science, Ewha Womans University, Seoul 120-750, Korea. E-mail: wwnam@ewha.ac.kr*

[b]*Department of Emerging Materials Science, DGIST, Daegu 711-873, Korea*

[c]*Picobiology Institute, Graduate School of Life Science, University of Hyogo, Hyogo 678-1297, Japan*

[d]*Department of Chemistry and Pharmacy, University of Erlangen-Nürnberg, 91058 Erlangen, Germany*

[e]*Stanford Synchrotron Radiation Lightsource, SLAC National Accelerator Laboratory, Menlo Park, CA 94025, USA. E-mail: ritis@slac.stanford.edu*

[f]*Department of Material and Life Science, Graduate School of Engineering, ALCA, Japan Science and Technology Agency (JST), Osaka University, Suita, Osaka 565-0871, Japan. E-mail: fukuzumi@chem.eng.osaka-u.ac.jp*

† Electronic supplementary information (ESI) available: Experimental section; synthesis and characterization data and kinetic details. See DOI: 10.1039/c3sc51864g

‡ These authors contributed equally to this work.

$Fe^{III}(O_2)]^+$ complex provided us with an opportunity to use this intermediate in the investigation of chemical and physical properties of the biologically important iron(III)–O_2 species.

Redox-inactive metal ions that function as Lewis acids are known to play pivotal roles in a variety of oxidation reactions by oxygen-containing metal complexes, including dioxygen activation/formation and functionalization of organic substrates. One notable example is a redox-inactive Ca^{2+} ion in the oxidation of water to dioxygen in the oxygen-evolving complex (OEC, a heteronuclear Mn_4CaO_5 cubane complex) of Photosystem II (PS II),[12–14] although the role of the Ca^{2+} ion in making the O–O bond has yet to be clarified.[15] In biomimetic studies, redox-inactive metal ions have shown remarkable effects on the reactivities of metal–oxo complexes in electron transfer, oxygen atom transfer, and C–H bond activation reactions.[16–26] It has been demonstrated that the binding of redox-inactive metal ions to the metal–oxo complexes changes their redox potentials, thereby increasing their oxidizing power that enhances reactivities of the metal–oxo species in oxidation reactions. The activation of dioxygen by metal complexes is also facilitated in the presence of redox-inactive metal ions (*e.g.*, Ca^{2+}).[27] Thus, the role(s) of redox-inactive metal ions is being unveiled in various oxidation/reduction reactions by oxygen-containing metal complexes.

Redox-inactive metal ions also bind to metal–peroxo complexes (*e.g.*, Ni–O_2 and Cu–O_2), and the peroxide O–O bond of the metal–peroxo complexes is cleaved by binding a second metal ion to give heterobimetallic $M(\mu\text{-}O)_2M'$ complexes.[28–31] In one case, a crystal structure of a nickel–peroxo complex binding potassium ion, [LNi(μ,η^2:η^2-O_2)K(solvent)], was successfully obtained.[32] However, reactions of nonheme iron(III)–peroxo complexes with redox-inactive metal ions have never been investigated, although crystal structures of iron porphyrin–O_2–copper complexes and mechanisms of the O–O bond cleavage of the intermediates have been intensively investigated as a chemical model of cytochrome *c* oxidase (C*c*O),[33–35] an enzyme that catalyzes the reduction of dioxygen to water *via* the formation of a presumed iron(III) porphyrin–O_2–copper(II) intermediate.[36,37] However, the final step of the catalytic cycle of C*c*O, which is the O–O bond activation of the iron porphyrin–O_2–copper intermediate to form iron(IV)–oxo and Cu(II) species, remains elusive.

As part of our ongoing efforts to understand the effects of redox-inactive metal ions on the chemical and physical properties of oxygen-containing metal complexes in enzymatic and biomimetic reactions, we have synthesized and characterized mononuclear nonheme iron(III)–peroxo complexes binding redox-inactive metal ions, $[(TMC)Fe^{III}(O_2)]^+$–M^{3+} (M^{3+} = Sc^{3+} and Y^{3+}). We have also shown that these $[(TMC)Fe^{III}(O_2)]^+$–M^{3+} complexes are reduced by one-electron donors (*e.g.*, ferrocene) and converted to the corresponding iron(IV)–oxo complex *via* O–O bond cleavage. The rates of O–O bond cleavage depend significantly on the Lewis acidity of the redox-inactive metal ions and the reduction potential of the electron donors. The overall mechanism of the O–O bond activation of the iron(III)–peroxo complexes by binding redox-inactive metal ions and specifically the role of the redox-inactive metal ions in facilitating the O–O cleavage are discussed as well.

Results and discussion

The iron(III)–peroxo complex, $[(TMC)Fe^{III}(O_2)]^+$ (**1**), which was prepared by reacting $[Fe^{II}(TMC)(CF_3SO_3)_2]$ with 5 equiv. H_2O_2 in the presence of 2 equiv. triethylamine in CF_3CH_2OH or CH_3CN at −40 °C,[9–11] was isolated as a solid and used for further reactions. Addition of 3 equiv. of scandium triflate, $Sc(CF_3SO_3)_3$, to a solution of **1** in acetone–CF_3CH_2OH (v/v = 3 : 1) at −40 °C immediately generated a purple intermediate (**2**–Sc) with an electronic absorption band at λ_{max} = 530 nm (Fig. 1a). Similarly, the reaction of **1** with 5 equiv. of yttrium triflate, $Y(CF_3SO_3)_3$, in acetone–CF_3CH_2OH (v/v = 3 : 1) at −40 °C afforded the generation of a purple intermediate (**2**–Y) with an electronic absorption band at λ_{max} = 560 nm (Fig. 1a). When the reactions were carried out in CH_3CN–CF_3CH_2OH (v/v = 1 : 1), addition of one equiv. of Sc^{3+} and Y^{3+} afforded the full conversion of **1** to **2**–Sc and **2**–Y, respectively (ESI, Fig. S1†). The intermediates **2**–Sc and **2**–Y were highly stable and persisted for several days at −40 °C, which allowed us to characterize them with various spectroscopic techniques, such as electron paramagnetic resonance (EPR) spectroscopy, electrospray ionization mass spectrometry (ESI MS), resonance Raman (rRaman) spectroscopy, and X-ray absorption spectroscopy/extended X-ray absorption fine structure (XAS/EXAFS).

The EPR spectra of the intermediates, **2**–Sc and **2**–Y, exhibit signals at g = 9.2, 5.0, and 3.8 for **2**–Sc and g = 8.8, 5.2, and 3.4 for **2**–Y (ESI, Fig. S2†), which are indicative of high-spin (S = 5/2) Fe(III) species.[38] The ESI MS of **2**–Sc exhibits a prominent ion peak at a mass-to-charge (m/z) ratio of 835.9966 (ESI, Fig. S3†), whose mass and isotope distribution pattern correspond to $[(TMC)Fe(O_2)Sc(CF_3SO_3)_3]^+$ (calculated m/z of 835.9989). The ESI MS of **2**–Y exhibits a prominent ion peak at m/z of 879.9496 (ESI, Fig. S4†), whose mass and isotope distribution pattern correspond to $[(TMC)Fe(O_2)Y(CF_3SO_3)_3]^+$ (calculated m/z of 879.9489).

The rRaman spectrum of the ^{16}O-labeled **2**–Sc in acetone-d_6, obtained by 515 nm excitation at −20 °C, shows two peaks with isotope shifts upon ^{18}O-substitution (Fig. 1b). The peak at 543 cm^{-1} shifts to 522 cm^{-1} with a $^{16,18}\Delta$ value of 21 cm^{-1} ($^{16,18}\Delta$ (calcd) = 21 cm^{-1}) and is assigned as the Fe–O stretching vibration.[39,40] The other isotopically sensitive peak at 807 cm^{-1} shifts to 761 cm^{-1} with a $^{16,18}\Delta$ value of 46 cm^{-1} ($^{16,18}\Delta$ (calcd) = 47 cm^{-1}) and is assigned as the O–O stretching vibration.[39,40] The Fe–O and O–O stretching vibrations for **2**–Y were observed at 540 and 799 cm^{-1}, respectively (Fig. 1b). Thus, the O–O stretching frequencies of **2**–Sc and **2**–Y indicate that the O_2 unit in **2**–Sc and **2**–Y retains the peroxo character, O_2^{2-}. Further, the O–O stretching frequencies of **2**–Sc (807 cm^{-1}) and **2**–Y (799 cm^{-1}) are smaller than that of **1** (825 cm^{-1}),[10,11] whereas the Fe–O stretching frequencies of **2**–Sc (543 cm^{-1}) and **2**–Y (540 cm^{-1}) are higher than that of **1** (487 cm^{-1})[10,11] (Fig. 1b). Furthermore, these values are significantly smaller than the Fe–O (658 cm^{-1}) and O–O (868 cm^{-1}) stretches in a high-spin end-on Fe(III)–hydroperoxo complex bearing the TMC ligand, $[(TMC)Fe^{III}(OOH)]^{2+}$ (**3**).[10,11]

A comparison of the k^3 weighted Fe K-edge EXAFS for **1** and its $Sc(CF_3SO_3)_3$ and $Y(CF_3SO_3)_3$ adducts, **2**–Sc and **2**–Y,

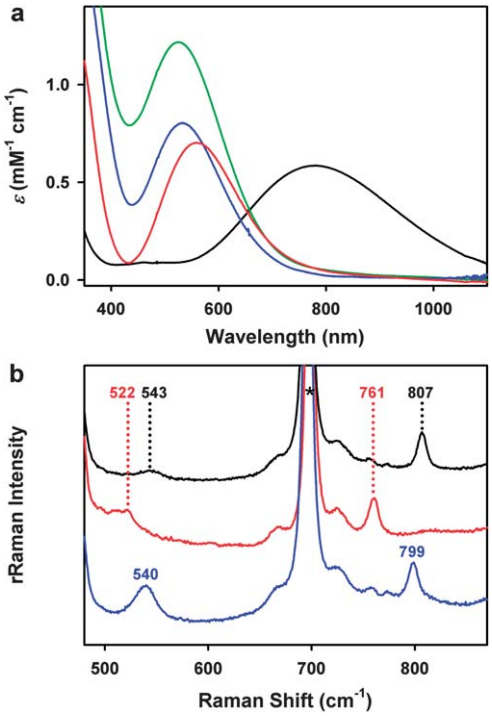

Fig. 1 (a) UV-vis spectral changes observed in the conversion of **1** (black line) to **2**–Sc (blue line) and **2**–Y (red line) upon addition of Sc^{3+} (3.0 mM) and Y^{3+} (3.0 mM) to the solution of **1** (1.0 mM), respectively, in acetone–CF_3CH_2OH (3 : 1) at −40 °C. UV-vis spectrum of $[(TMC)Fe^{III}(OOH)]^{2+}$ (**3**, green line) is shown for comparison. (b) Resonance Raman spectra of **2**–Sc–^{16}O (8.0 mM; black line), **2**–Sc–^{18}O (8.0 mM; red line), and **2**–Y–^{16}O (8.0 mM; blue line) obtained upon excitation at 515 nm in acetone-d_6 at −20 °C. **2**–Sc–^{16}O and **2**–Sc–^{18}O were generated upon addition of Sc^{3+} ions to solutions of isolated $[(TMC)Fe^{III}(^{16}O_2)]^+$ and $[(TMC)Fe^{III}(^{18}O_2)]^+$, respectively. **2**–Y–$^{16}O$ was generated upon addition of Y^{3+} ions to the solution of an isolated $[(TMC)Fe^{III}(^{16}O_2)]^+$ complex. The peak marked with an "asterisk" is ascribed to acetone-d_6 solvent.

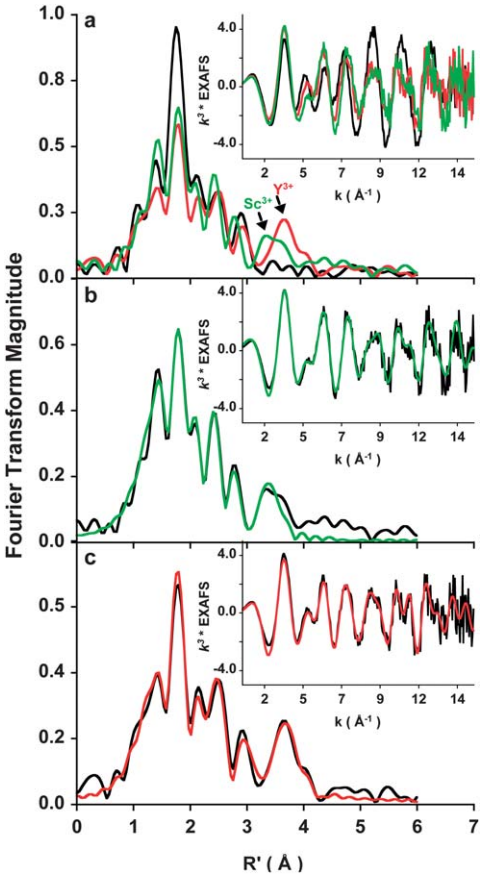

Fig. 2 (a) A comparison of the non phase-shift corrected Fourier transforms and the corresponding EXAFS data (inset) for **1** (black line), **2**–Sc (green line), and **2**–Y (red line). (b) FEFF best-fit (black line) to **2**–Sc (green line). (c) FEFF best-fit (black line) to **2**–Y (red line).

respectively, along with their non-phase shift corrected Fourier transforms (k = 1–15 $Å^{-1}$) is shown in Fig. 2a. The data show that the first shells of **2**–Sc and **2**–Y are diminished in intensity relative to **1**, indicating a perturbation in the first shell distances. Additionally, both **2**–Sc and **2**–Y have significant intensity between R′ 3–4 Å, which is absent in **1**, indicating heavy atom coordination. FEFF[41] fits to the data for **2**–Sc and **2**–Y are presented in Fig. 2b and c and ESI, Table S1.† The best fits to the data of **2**–Sc and **2**–Y indicate a six-coordinate first shell in both complexes with two short Fe–O distances at 1.98 and 1.97 Å, respectively, and four longer Fe–N distances at 2.17 and 2.19 Å, respectively. The second shell is fit with single and multiple scattering components from the TMC ligand. The data for **2**–Sc are best fit when a Fe–Sc and its corresponding multiple scattering contribution, Fe–O–Sc, are included. The Fe–Sc distance optimizes to 3.8 Å. In **2**–Y, inclusion of Fe–Y and Fe–O–Y components is necessary to obtain a good fit and the Fe–Y distance optimizes to be 4.0 Å. Thus, the EXAFS analyses show that both **2**–Sc and **2**–Y are side-on bound Fe(III)–O_2 species complexed with Sc^{3+} and Y^{3+}, respectively. A comparison with the EXAFS data of **1** shows that the first shell distances of **2**–Sc and **2**–Y are perturbed by metal ion binding, with the Fe–O bonds longer (by 0.06 and 0.05 Å, respectively) and the Fe–N bond distances slightly shorter (by 0.04 and 0.02 Å, respectively).

To shed further light on the structural basis of Sc^{3+} and Y^{3+} bound to **1** and understand the structural differences, spin unrestricted density functional theory calculations were performed on $[(TMC)Fe(O_2)]^+$, $[(TMC)Fe(O_2)–Sc(CF_3SO_3)_3]^+$, and $[(TMC)Fe(O_2)–Y(CF_3SO_3)_3]^+$. All three converged to side-on bound Fe(III)–O_2 systems (see Fig. 3 for metrical parameters and ESI, Table S2† for spin populations and Mulliken[42] charges). As can be seen from the Mayer[43] bond orders, upon binding to the innocent metal ion (*e.g.*, Sc^{3+}/Y^{3+}), both the O–O and Fe–O bonds in **1** become weaker. This is because the Fe–O_2 orbital overlap is significantly diminished, as seen in the decrease in O_2 Mulliken populations in the d_{xy} and d_{xz} orbitals. This decrease restores electron density into the O_2 π^* orbitals and weakens the O–O bond, as is also seen in the increase in the calculated O–O distance from 1.42 in **1** to 1.49 Å in both **2**–Sc and **2**–Y and the decrease in the O–O stretching frequency from 825 cm^{-1} in **1** to 807 cm^{-1} in **2**–Sc and 799 cm^{-1} in **2**–Y in rRaman experiments (Fig. 1b). However, it is of interest to note that the experimental Fe–O stretching frequencies for **2**–Sc and **2**–Y are higher than that of **1** (*vide supra*), even though EXAFS analysis

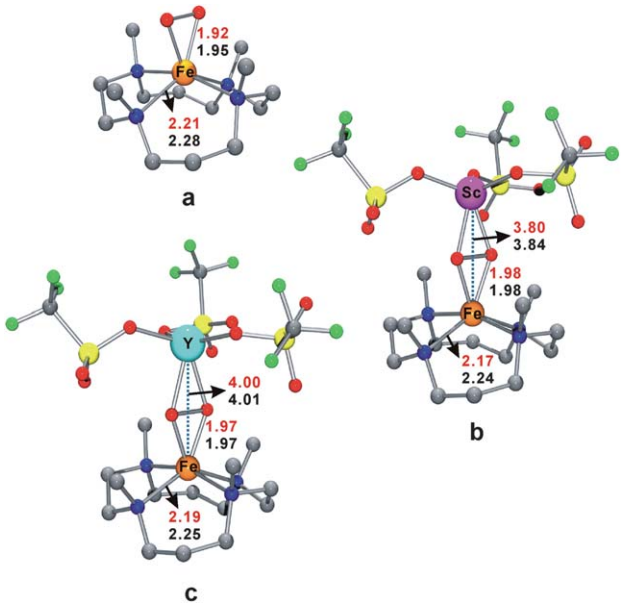

Fig. 3 DFT-optimized structures of **1** (a), **2**–Sc (b), and **2**–Y (c). The distances obtained from EXAFS (red) are shown for comparison to the DFT distances (black). The average Fe–N distances from DFT are compared to experimental data. Atom colours: Fe, orange; N, blue; O, red; S, yellow; C, gray; F, green; Sc, purple; Y, cyan.

shows that the M–O bonds become longer upon binding of Sc^{3+}/Y^{3+}. To understand this, numerical frequency calculations were performed on **1**, **2**–Sc, and **2**–Y and the values of 430 cm^{-1}, 494 cm^{-1}, and 503 cm^{-1}, respectively, reproduce the experimental trend. In **2**–Sc and **2**–Y, the Fe–O mode is kinematically coupled with the Sc/Y–O mode, which results in the observed higher frequency, even though the Fe–O bond is weaker.

In this section, we have shown the synthesis of mononuclear nonheme iron(III)–peroxo complexes binding redox-inactive metal ions. Based on the spectroscopic characterization of the iron(III)–peroxo complexes binding Sc^{3+} and Y^{3+} ions presented above, we were able to conclude unambiguously that **2**–Sc and **2**–Y are mononuclear iron(III)–peroxo complexes binding a peroxo ligand in a side-on η^2 fashion between two metal ions, $[(TMC)Fe^{III}–(\mu,\eta^2:\eta^2\text{-}O_2)–M^{III}(CF_3SO_3)_3]^+$ (see Fig. 3).

As mentioned above, the $[(TMC)Fe^{III}(O_2)]^+$–M^{3+} (**2**–M) species, **2**–Sc and **2**–Y, are stable for several days in CH_3CN–CF_3CH_2OH (1 : 1) at −40 °C. Interestingly, addition of one equiv. of ferrocene (Fc) to solutions of **2**–Sc and **2**–Y resulted in the immediate disappearance of the absorption peaks corresponding to **2**–Sc at 535 nm and **2**–Y at 570 nm, with the concomitant appearance of absorption peaks corresponding to $[(TMC)Fe^{IV}(O)]^{2+}$ (**4**)[44] at 820 nm and ferrocenium cations (Fc^+)[20] at 620 nm (Fig. 4a for the reaction of **2**–Sc and ESI, Fig. S5† for the reaction of **2**–Y). Well-defined isosbestic points were observed at 713 and 759 nm in the titration reactions of **2**–Sc and **2**–Y, respectively (Fig. 4a and ESI, Fig. S5†). These results demonstrate unambiguously that one-electron transfer from Fc to **2**–Sc and **2**–Y resulted in the formation of **4** *via* the O–O bond cleavage of the peroxide ligand (*vide infra*). It should be noted that the iron(III)–peroxo complex, $[(TMC)Fe^{III}(O_2)]^+$ (**1**), did not react with Fc, indicating that the electron transfer from Fc to **2**–M was facilitated by the binding of redox-inactive metal ions to **1**. It should also be noted that the iron(IV)–oxo complex, $[(TMC)Fe^{IV}(O)]^{2+}$ (**4**), which was produced in the reaction of **2**–M and Fc, was not reduced by Fc under the reaction conditions,[45] suggesting that the reactivity of **2**–M is much greater than that of **4** with Fc in the electron-transfer (ET) reaction (*vide infra*).

Then, the rates of the electron transfer from Fc to **2**–Sc and **2**–Y were determined under the pseudo-first-order reaction conditions (*e.g.*, with >10 equiv. of Fc to **2**–M). First-order rate constants, determined by the pseudo-first-order fitting of the kinetic data for the decay of **2**–Sc and **2**–Y (Fig. 4b and ESI, Fig. S6†), increased linearly with the increase of the Fc concentration, and the second-order rate constants (k_{et}), such as 1.6×10^4 M^{-1} s^{-1} for **2**–Sc and 5.8×10 M^{-1} s^{-1} for **2**–Y at −40 °C, were determined from the slopes of linear plots of k_{obs} *vs.* [Fc] (ESI, Fig. S6a and S7b†). The results clearly indicate that the reaction rates depend on the Lewis acidity of the metal ions in **2**–M; the stronger the Lewis acidity of the binding metal ion is, the faster is the ET reaction between **2**–M and Fc. Similarly, the k_{et} values of electron transfer from other Fc derivatives, such as octamethylferrocene (Me_8Fc), dimethylferrocene (Me_2Fc), bromoferrocene (BrFc), acetylferrocene

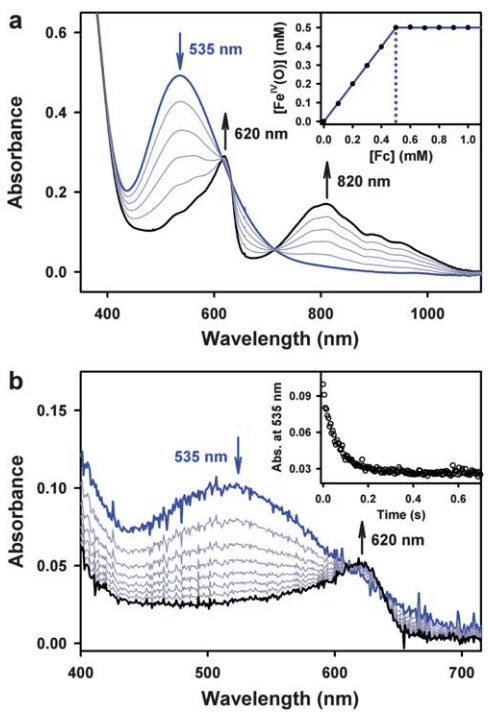

Fig. 4 (a) UV-vis spectral changes showing the disappearance of **2**–Sc at 535 nm and the formation of $[(TMC)Fe^{IV}(O)]^{2+}$ (**4**) at 820 nm and Fc^+ ions at 620 nm by addition of Fc (0.0–1.0 mM) to a solution of **2**–Sc (0.50 mM) in increments of 0.2 equiv. in CH_3CN–CF_3CH_2OH (1 : 1) at −40 °C. Inset shows the spectroscopic titration at 820 nm for the formation of **4** as a function of the equiv. of Fc added to the solution of **2**–Sc (0.50 mM) in increments of 0.2 equiv. (b) Spectral changes observed in the electron transfer from Fc (1.0 mM) to **2**–Sc (0.10 mM) in CH_3CN–CF_3CH_2OH (1 : 1) at −40 °C. Inset shows the time course monitored at 535 nm for the decay of **2**–Sc.

(AcFc), and dibromoferrocene (Br_2Fc), to **2**–M were determined and listed in Table S3† (also see Fig. S6 and S7† for the linear plots for the determination of k_{et}). In all of the reactions, the k_{et} values of **2**–Sc were greater than those of **2**–Y (*i.e.*, k_{et} for **2**–Sc > k_{et} for **2**–Y), demonstrating again that **2**–M binding a metal ion with stronger Lewis acidity is more reactive in the ET reaction. In addition, the reaction rates were different depending on the oxidation potential of the electron donors; the conversion of **2**–M to **4** is faster with electron donors having lower oxidation potential (*i.e.*, Me_8Fc > Me_2Fc > Fc > BrFc > AcFc > Br_2Fc) (see ESI, Table S3 and ESI, Fig. S6 and S7†). These results imply that the electron transfer from the electron donor to **2**–M determines the reaction rate (*vide infra*).

The one-electron reduction potentials (E_{red}) and reorganization energies of electron transfer (λ) of **2**–Sc and **2**–Y were then estimated to understand the fundamental ET properties of the iron(III)–peroxo complexes binding redox-inactive metal ions. Since the reduction of **2**–Sc and **2**–Y by the electron donors resulted in a rapid O–O bond cleavage to yield $[(TMC)Fe^{IV}(O)]^{2+}$ (**4**), the E_{red} values of **2**–Sc and **2**–Y could not be determined by a conventional cyclic voltammetry method. We therefore estimated the E_{red} values by analyzing the driving force dependence of k_{et} for the irreversible ET reduction of **2**–Sc and **2**–Y using the Marcus theory of electron transfer.[46] First, the k_{et} values were converted to the activation free energies ($\Delta G_{et}^{\ddagger}$) using eqn (1), where Z is the frequency factor taken as 1×10^{11} M^{-1} s^{-1}. The calculated $\Delta G_{et}^{\ddagger}$ values are listed in ESI, Table S3.† According to the Marcus theory of electron transfer, $\Delta G_{et}^{\ddagger}$ is given as a function of ΔG_{et} (free energy change of electron transfer) and λ, as shown in eqn (2). Since ΔG_{et} is given as the difference between the one-electron oxidation potential of an electron donor (E_{ox}) and the one-electron reduction potential of $[(TMC)Fe^{III}(O_2)]^{+}$–M^{n+} (E_{red}) (*i.e.*, $\Delta G_{et} = e(E_{ox} - E_{red})$), eqn (3) is rewritten as a linear correlation between $(\Delta G_{et}^{\ddagger})^{1/2}$ and E_{ox} (eqn (4)),[46] and plots of $(\Delta G_{et}^{\ddagger})^{1/2}$ *vs.* E_{ox} for electron transfer from Fc and Fc derivatives to **2**–Sc and **2**–Y are shown in Fig. 5.

$$k_{et} = Z\exp(-\Delta G_{et}^{\ddagger}/k_B T) \quad (1)$$

$$\Delta G_{et}^{\ddagger} = (\lambda/4)(1 + \Delta G_{et}/\lambda)^2 \quad (2)$$

$$(\Delta G_{et}^{\ddagger})^{1/2} = (\lambda/4)^{1/2}(1 + e(E_{ox} - E_{red})/\lambda) \quad (3)$$

$$(\Delta G_{et}^{\ddagger})^{1/2} = (1/4\lambda)^{1/2} eE_{ox} + (1/4\lambda)^{1/2}(\lambda - eE_{red}) \quad (4)$$

From the slopes and intercepts in Fig. 5, the E_{red} values of **2**–Sc and **2**–Y were estimated to be 0.40 and 0.16 V *vs.* SCE, respectively, and the λ values of both **2**–Sc and **2**–Y were evaluated to be 1.29 eV. The λ values of both **2**–Sc and **2**–Y were evaluated to be virtually the same as 1.29 eV, which is significantly smaller than that of the iron(IV)–oxo complex (**4**, $\lambda = 2.37$ eV). The smaller λ values of **2**–Sc and **2**–Y, as compared with **4**, may result from the difference in the bond order between the peroxo complexes (*e.g.*, single bond) and the oxo complex (*e.g.*, double bond), since the reduction of the oxo double bond results in the significant elongation of the Fe–O bond, which is accompanied by a larger reorganization energy as compared with those of the peroxo complexes (**2**–Sc and **2**–Y). The same λ values of **2**–Sc and **2**–Y suggest that the electron-transfer reduction occurs at the metal center and that the difference in the Fe–O bond distance caused by the electron-transfer reduction remains virtually the same between **2**–Sc and **2**–Y. The higher E_{red} value of **2**–Sc than that of **2**–Y results from the stronger Lewis acidity of Sc^{3+} than that of Y^{3+},[47] which further indicates that **2**–Sc is more electron deficient than **2**–Y. As a result, **2**–Sc is reduced faster than **2**–Y by the electron donors, as discussed above. To the best of our knowledge, this is the first time the fundamental ET properties of iron(III)–peroxo complexes binding redox-inactive metal ions have been reported (see Fig. S8† for the k_{et} value of **4** and the comparison of the E_{red}, λ, and k_{et} values of **2**–Sc, **2**–Y, and **4** in ESI†).

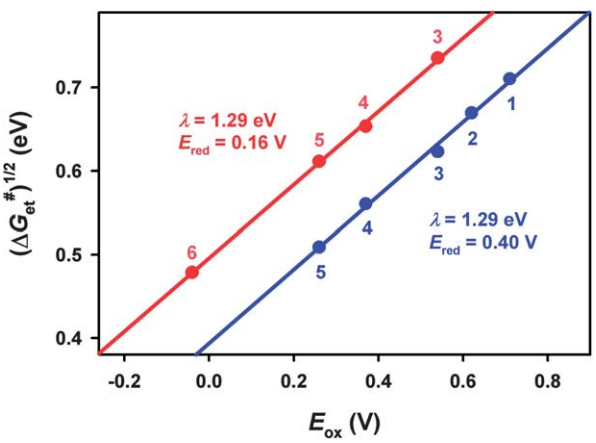

Fig. 5 Plots of $(\Delta G_{et})^{1/2}$ *vs.* E_{ox} values of Fc derivatives [Br_2Fc (1), AcFc (2), BrFc (3), Fc (4), Me_2Fc (5), and Me_8Fc (6)] in the electron transfer from Fc derivatives to **2**–Sc (blue circles) and **2**–Y (red circles) in CH_3CN–CF_3CH_2OH (1 : 1) at −40 °C.

Conclusions

In conclusion, we have reported for the first time the effects of redox-inactive metal ions on the chemical properties of a mononuclear nonheme iron(III)–peroxo complex in ET reactions. While the iron(III)–peroxo complex, $[(TMC)Fe^{III}(O_2)]^{+}$ (**1**),

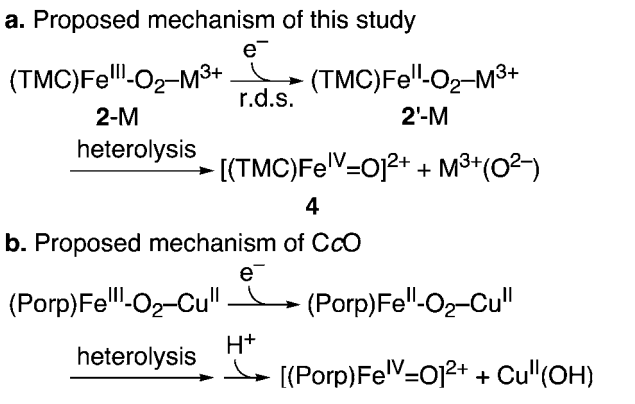

Scheme 1

cannot be reduced by electron donors (*e.g.*, Fc derivatives), the iron(III)–peroxo complexes binding redox-inactive metal ions, $[(TMC)Fe^{III}(O_2)]^+$–M^{3+} (**2**–M, $M^{3+} = Sc^{3+}$ and Y^{3+}), are reduced by the electron donors, resulting in the peroxide O–O bond cleavage of **2**–M to form the corresponding iron(IV)–oxo complex, $[(TMC)Fe^{IV}(O)]^{2+}$ (**4**) (Scheme 1; see ESI, Fig. S9† for the ESI MS spectrum of the $M^{3+}(O)$ product). We have also shown that the rates of the conversion of **2**–M to **4** are dependent on the Lewis acidity of the redox-inactive metal ions and concentration and oxidation potential of the electron donors.[48] These results indicate that the reduction of **2**–M by electron donors to form the one-electron reduced species (*i.e.*, $[(TMC)Fe^{II}(O_2)]$–M^{3+} (**2′**–M)) is the rate-determining step (r.d.s.), followed by a rapid heterolytic O–O bond cleavage of the peroxide ligand of **2′**–M that results in the formation of **4** (Scheme 1a). The fundamental ET properties of **2**–M, such as the reduction potential and the reorganization energy in ET reactions, have also been estimated and compared with those of the corresponding iron(IV)–oxo complex (**4**). The faster electron transfer rates and the greater reactivities of **2**–M are ascribed to the smaller reorganization energy of **2**–M than that of **4** (ESI, Fig. S8†). In addition, the linear plots of $(\Delta G_{et}^{\ddagger})^{1/2}$ *vs.* E_{ox} shown in Fig. 5 support the proposed mechanism that the one-electron reduction of **2**–M to $[(TMC)Fe^{II}(O_2)]$–M^{n+} is the r.d.s. (Scheme 1a). Finally, the observation that one-electron reduction of the $[(TMC)Fe^{III}$–$O_2]$–M^{3+} species affords the formation of the corresponding iron(IV)–oxo species leads us to propose that the iron(III) porphyrin–O_2–Cu(II) intermediate at the active site of C*c*O is reduced by one-electron to iron(II) porphyrin–O_2–Cu(II), followed by the heterolytic O–O bond cleavage of the iron(II) porphyrin–O_2–Cu(II) moiety to give the $S = 1$ Fe(IV)–oxo and Cu(II) species (Scheme 1b).[33,35–37,49] In this regard, the Cu(II) ion in the iron(III) porphyrin–O_2–Cu(II) intermediate in C*c*O may function as a Lewis acid that facilitates the one-electron reduction of iron(III) porphyrin–O_2–Cu(II) (Scheme 1b), although no experimental evidence supporting our assertion has been obtained so far. Detailed mechanistic studies, including density functional theory (DFT) calculations for the one-electron reduction and O–O bond cleavage steps of the nonheme iron(III)–peroxo complex binding redox-inactive metal ions, are underway in this laboratory to correlate these biomimetic observations to enzymatic reactions (*e.g.*, C*c*O).[50,51]

Acknowledgements

The research was supported by KOSEF/MEST of Korea through the CRI (2-2012-1794-001-1 to W.N.), GRL (2010-00353 to W.N.) and WCU (R31-2008-000-10010-0 to W.N. and S.F.) programs, and the R&D (13-BD-0403 and 2013K2A2A4000610 to J.C.) programs of the MEST of Korea, and Grants-in-Aid (no. 20108010 to S.F.) and the Global COE program and Priority Area (no. 20050029) (T.O.) from MEXT of Japan. I.I.B. and O.T. gratefully acknowledge support through the "Solar Technologies Go Hybrid" initiative of the German Federate State of Bavaria. XAS data were measured at the Stanford Synchrotron Radiation Lightsource (SSRL), a Directorate of SLAC National Accelerator Laboratory and an Office of Science User Facility operated for the U.S. Department of Energy Office of Science by Stanford University. The SSRL Structural Molecular Biology Program is supported by the National Institutes of Health and by the Department of Energy, Office of Biological and Environmental Research (BER). The publication was partially supported by National Institutes of Health (NIH) Grant number 5 P41 RR001209.

Notes and references

1 (*a*) E. I. Solomon, S. D. Wong, L. V. Liu, A. Decker and M. S. Chow, *Curr. Opin. Chem. Biol.*, 2009, **13**, 99–113; (*b*) M. L. Neidig and E. I. Solomon, *Chem. Commun.*, 2005, 5843–5863; (*c*) E. I. Solomon, T. C. Brunold, M. I. Davis, J. N. Kemsley, S. K. Lee, N. Lehnert, F. Neese, A. J. Skulan, Y. S. Yang and J. Zhou, *Chem. Rev.*, 2000, **100**, 235–350.

2 E. G. Kovaleva and J. D. Lipscomb, *Nat. Chem. Biol.*, 2008, **4**, 186–193.

3 E. G. Kovaleva, M. B. Neibergall, S. Chakrabarty and J. D. Lipscomb, *Acc. Chem. Res.*, 2007, **40**, 475–483.

4 M. M. Abu-Omar, A. Loaiza and N. Hontzeas, *Chem. Rev.*, 2005, **105**, 2227–2252.

5 E. G. Kovaleva and J. D. Lipscomb, *Science*, 2007, **316**, 453–457.

6 G. Katona, P. Carpentier, V. Nivière, P. Amara, V. Adam, J. Ohana, N. Tsanov and D. Bourgeois, *Science*, 2007, **316**, 449–453.

7 A. Karlsson, J. V. Parales, R. E. Parales, D. T. Gibson, H. Eklund and S. Ramaswamy, *Science*, 2003, **299**, 1039–1042.

8 J. Cho, R. Sarangi and W. Nam, *Acc. Chem. Res.*, 2012, **45**, 1321–1330.

9 J. Annaraj, Y. Suh, M. S. Seo, S. O. Kim and W. Nam, *Chem. Commun.*, 2005, 4529–4531.

10 F. Li, K. K. Meier, M. A. Cranswick, M. Chakrabarti, K. M. Van Heuvelen, E. Münck and L. Que, Jr, *J. Am. Chem. Soc.*, 2011, **133**, 7256–7259.

11 J. Cho, S. Jeon, S. A. Wilson, L. V. Liu, E. A. Kang, J. J. Braymer, M. H. Lim, B. Hedman, K. O. Hodgson, J. S. Valentine, E. I. Solomon and W. Nam, *Nature*, 2011, **478**, 502–505.

12 Y. Umena, K. Kawakami, J.-R. Shen and N. Kamiya, *Nature*, 2011, **473**, 55–61.

13 J. S. Kanady, E. Y. Tsui, M. W. Day and T. Agapie, *Science*, 2011, **333**, 733–736.

14 (*a*) E. Y. Tsui, R. Tran, J. Yano and T. Agapie, *Nat. Chem.*, 2013, **5**, 293–299; (*b*) J. S. Kanady, J. L. Mendoza-Cortes, E. Y. Tsui, R. J. Nielsen, W. A. Goddard and T. Agapie, *J. Am. Chem. Soc.*, 2013, **135**, 1073–1082.

15 V. K. Yachandra and J. Yano, *J. Photochem. Photobiol., B*, 2011, **104**, 51–59.

16 C. G. Miller, S. W. Gordon-Wylie, C. P. Horwitz, S. A. Strazisar, D. K. Peraino, G. R. Clark, S. T. Weintraub and T. J. Collins, *J. Am. Chem. Soc.*, 1998, **120**, 11540–11541.

17 S.-M. Yiu, Z.-B. Wu, C.-K. Mak and T.-C. Lau, *J. Am. Chem. Soc.*, 2004, **126**, 14921–14929.

18 S.-M. Yiu, W.-L. Man and T.-C. Lau, *J. Am. Chem. Soc.*, 2008, **130**, 10821–10827.

19 H. Du, P.-K. Lo, Z. Hu, H. Liang, K.-C. Lau, Y.-N. Wang, W. W. Y. Lam and T.-C. Lau, *Chem. Commun.*, 2011, **47**, 7143–7145.
20 S. Fukuzumi, Y. Morimoto, H. Kotani, P. Naumov, Y.-M. Lee and W. Nam, *Nat. Chem.*, 2010, **2**, 756–759.
21 Y. Morimoto, H. Kotani, J. Park, Y.-M. Lee, W. Nam and S. Fukuzumi, *J. Am. Chem. Soc.*, 2011, **133**, 403–405.
22 J. Park, Y. Morimoto, Y.-M. Lee, W. Nam and S. Fukuzumi, *J. Am. Chem. Soc.*, 2011, **133**, 5236–5239.
23 J. Chen, Y.-M. Lee, K. M. Davis, X. Wu, M. S. Seo, K.-B. Cho, H. Yoon, Y. J. Park, S. Fukuzumi, Y. N. Pushkar and W. Nam, *J. Am. Chem. Soc.*, 2013, **135**, 6388–6391.
24 F. F. Pfaff, S. Kundu, M. Risch, S. Pandian, F. Heims, I. Pryjomska-Ray, P. Haack, R. Metzinger, E. Bill, H. Dau, P. Comba and K. Ray, *Angew. Chem., Int. Ed.*, 2011, **50**, 1711–1715.
25 P. Leeladee, R. A. Baglia, K. A. Prokop, R. Latifi, S. P. de Visser and D. P. Goldberg, *J. Am. Chem. Soc.*, 2012, **134**, 10397–10400.
26 S. Fukuzumi, *Coord. Chem. Rev.*, 2013, **257**, 1564–1575.
27 (*a*) Y. J. Park, J. W. Ziller and A. S. Borovik, *J. Am. Chem. Soc.*, 2011, **133**, 9258–9261; (*b*) Y. J. Park, S. A. Cook, N. S. Sickerman, Y. Sano, J. W. Ziller and A. S. Borovik, *Chem. Sci.*, 2013, **4**, 717.
28 M. T. Kieber-Emmons and C. G. Riordan, *Acc. Chem. Res.*, 2007, **40**, 618–625.
29 (*a*) S. Yao and M. Driess, *Acc. Chem. Res.*, 2012, **45**, 276–287; (*b*) S. Yao, C. Herwig, Y. Xiong, A. Company, E. Bill, C. Limberg and M. Driess, *Angew. Chem., Int. Ed.*, 2010, **49**, 7054–7058.
30 I. Garcia-Bosch, X. Ribas and M. Costas, *Eur. J. Inorg. Chem.*, 2012, 179–187.
31 S. Kundu, F. F. Pfaff, E. Miceli, I. Zaharieva, C. Herwig, S. Yao, E. R. Farquhar, U. Kuhlmann, E. Bill, P. Hildebrandt, H. Dau, M. Driess, C. Limberg and K. Ray, *Angew. Chem., Int. Ed.*, 2013, **52**, 5622–5626.
32 S. Yao, Y. Xiong, M. Vogt, H. Grützmacher, C. Herwig, C. Limberg and M. Driess, *Angew. Chem., Int. Ed.*, 2009, **48**, 8107–8110.
33 E. E. Chufán, S. C. Puiu and K. D. Karlin, *Acc. Chem. Res.*, 2007, **40**, 563–572.
34 (*a*) T. Chishiro, Y. Shimazaki, F. Tani, Y. Tachi, Y. Naruta, S. Karasawa, S. Hayami and Y. Maeda, *Angew. Chem., Int. Ed.*, 2003, **42**, 2788–2791; (*b*) J.-G. Liu, Y. Naruta and F. Tani, *Angew. Chem., Int. Ed.*, 2005, **44**, 1836–1840.
35 M. T. Kieber-Emmons, M. F. Qayyum, Y. Li, Z. HalimeK, O. Hodgson, B. Hedman, K. D. Karlin and E. I. Solomon, *Angew. Chem., Int. Ed.*, 2012, **51**, 168–172.
36 V. R. I. Kaila, M. I. Verkhovsky and M. Wikström, *Chem. Rev.*, 2010, **110**, 7062–7081.
37 J. P. Collman, N. K. Devaraj, R. A. Decréau, Y. Yang, Y.-L. Yan, W. Ebina, T. A. Eberspacher and C. E. D. Chidsey, *Science*, 2007, **315**, 1565–1568.
38 C. E. MacBeth, R. Gupta, K. R. Mitchell-Koch, V. G. Young, Jr, G. H. Lushington, W. H. Thompson, M. P. Hendrich and A. S. Borovik, *J. Am. Chem. Soc.*, 2004, **126**, 2556–2567.
39 J.-J. Girerd, F. Bense and A. J. Simaan, *Struct. Bonding*, 2000, **97**, 145–177.
40 T. Ohta, J.-G. Liu and Y. Naruta, *Coord. Chem. Rev.*, 2013, **257**, 407–413.
41 J. J. Rehr, J. Mustre de Leon, S. I. Zabinsky and R. C. Albers, *J. Am. Chem. Soc.*, 1991, **113**, 5135–5140.
42 R. S. Mulliken, *J. Chem. Phys.*, 1955, **23**, 1833–1840.
43 I. Mayer, *Chem. Phys. Lett.*, 1983, **97**, 270–274.
44 J.-U. Rohde, J.-H. In, M. H. Lim, W. W. Brennessel, M. R. Bukowski, A. Stubna, E. Münck, W. Nam and L. Que, Jr, *Science*, 2003, **299**, 1037–1039.
45 Y.-M. Lee, H. Kotani, T. Suenobu, W. Nam and S. Fukuzumi, *J. Am. Chem. Soc.*, 2008, **130**, 434–435.
46 (*a*) S. Fukuzumi, C. L. Wong and J. K. Kochi, *J. Am. Chem. Soc.*, 1980, **102**, 2928–2939; (*b*) S. Fukuzumi and J. K. Kochi, *Bull. Chem. Soc. Jpn.*, 1983, **56**, 969–979.
47 (*a*) S. Fukuzumi and K. Ohkubo, *Chem.–Eur. J.*, 2000, **6**, 4532–4535; (*b*) S. Fukuzumi and K. Ohkubo, *J. Am. Chem. Soc.*, 2002, **124**, 10270–10271.
48 This is classified as metal ion-coupled electron transfer: (*a*) S. Fukuzumi, *Prog. Inorg. Chem.*, 2009, **56**, 49–153; (*b*) S. Fukuzumi, K. Ohkubo and Y. Morimoto, *Phys. Chem. Chem. Phys.*, 2012, **14**, 8472–8484.
49 M. T. Kieber-Emmons, Y. Li, Z. Halime, K. D. Karlin and E. I. Solomon, *Inorg. Chem.*, 2011, **50**, 11777–11786.
50 Preliminary results on the synthesis and characterization of $[(TMC)Fe^{II}(O_2)]$–Sc^{3+} and –Y^{3+} complexes and the metal ion effect on the O–O bond activation have been reported by Nam and co-workers at the *Seventh International Conference on Porphyrins and Phthalcyanines (ICPP-7)* held in Jeju, Korea on July 1–7, 2012 and at the *6th Asian Biological Inorganic Chemistry Conference (AsBIC VI)* held in Hong Kong on November 5–8, 2012.
51 A report on $[(TMC)Fe^{II}(O_2)]$–Sc^{3+} as an intermediate in the formation of $[(TMC)Fe^{IV}(O)]^{2+}$ *via* O–O bond cleavage was published on June 26, 2013. See: F. Li, K. M. Van Heuvelen, K. K. Meier, E. Münck and L. Que, Jr, *J. Am. Chem. Soc.*, 2013, **135**, 10198–10201.